AIAA JOURNAL
Vol. 31, No. 8, August 1993

Numerical Investigation of Subsonic and Supersonic Asymmetric Vortical Flow

K. J. Vanden* and D. M. Belk†
Wright Laboratory, Armament Directorate, Eglin Air Force Base, Florida 32542

The high angle of attack flow about a slender body in supersonic and subsonic flow was computed for an angle of attack of 38.5 deg to study the phenomena associated with vortex asymmetry. A laminar thin-layer Navier-Stokes algorithm was used to determine whether vortex asymmetry in numerical computations is the result of a numerically induced perturbation or a property of the governing equations. The fully upwind code used in this study was symmetric in the crossflow plane to 12 orders of magnitude, the level of roundoff error on the Cray Y-MP. It was found that, with a completely symmetric grid and algorithm with respect to the crossflow plane, a bump was needed to perturb the flow to asymmetry. When the bump was taken away, the flow returned to a symmetric state. This corroborates the previous assertion of other investigators that vortex asymmetry at high angles of attack on slender bodies is due to a convective instability.

Introduction

THERE is a great deal of current interest in highly maneuverable aircraft capable of controlled flight at very high angles of attack. An understanding of the formation and structure of the vortices that tend to dominate these flowfields is critical. In particular, the formation of asymmetric vortices from very nearly symmetric bodies can introduce sizable side forces and yawing moments that must be either counteracted or, if possible, used to help control the flight of the body. Most recent studies of asymmetric vortical flow from slender bodies have quite appropriately concerned themselves with low Mach number flow, since few aircraft could withstand the enormous loads associated with high angle of attack flight at supersonic Mach numbers. The design of future air-to-air missiles, however, could benefit from a better understanding of high angle of attack supersonic flight.

The formation of asymmetric vortices over a symmetric ogive cylinder in supersonic flow is studied in this paper. A convincing argument has been made by Degani[1] that for subsonic laminar flow over an ogive cylinder the formation of asymmetric vortices involves a convective instability and requires an asymmetric upstream disturbance. Another possibility for formation of asymmetric vortices is a bifurcation type instability[2] associated with the existence of multiple steady-state solutions. A computational study by Siclari[3] has shown that supersonic conical flow naturally exhibits a range of bifurcated solutions without requiring imposition of a viscous separation model, geometric perturbation, or asymmetric boundary condition. Previous supersonic ogive-cylinder calculations by Vanden[4] yielded asymmetric flow without the introduction of any geometric or initial asymmetry. These calculations used a fully upwind finite volume scheme with a two-pass implicit approximate factorization that introduced an asymmetric error in the transient solution. Here we have developed an algorithm based on the same fully upwind explicit flux evaluation, but with an implicit two-pass approximate factorization that is symmetric in the crossflow plane. Using this code, flow symmetry is maintained until some perturbation is introduced. Results of numerical experiments for supersonic ogive-cylinder flow, similar to those of Degani[1] for subsonic flow, are presented to determine whether asymmetric vortical flow about a fully laminar supersonic ogive cylinder is due to a convective instability or a bifurcation. A small bump near the nose of the ogive is used to trigger the asymmetry. The sensitivity of the vortical flow structure to the mechanism triggering the asymmetry is studied by comparing the asymmetric flow due to variations in the numerical algorithm with the asymmetries arising from the more physically realistic case of a bump on the nose calculated by the symmetric algorithm. The study of the similarity or dissimilarity between supersonic and subsonic vortical flow is then carried further by comparing the structure, or topology, of the three-dimensional asymmetric vortical flow for both cases.

Presented as Paper 91-2869 at the AIAA Atmospheric Flight Mechanics Conference, New Orleans, LA, Aug. 12–14, 1991; received Feb. 10, 1992; revision received Dec. 23, 1992; accepted for publication Dec. 31, 1992.

*Research Scientist, Computational Fluid Dynamics Section, Aerodynamics Branch, Weapon Flight Mechanics Division. Member AIAA.

†Senior Research Scientist, Computational Fluid Dynamics Section, Aerodynamics Branch, Weapon Flight Mechanics Division. Associate Fellow AIAA.

Theoretical Background

Governing Equations and Numerical Algorithm

Steady-state solutions to these equations were computed with the Eagle code developed jointly by Mississippi State University and Wright Laboratory, Armament Directorate. The thin-layer version of the Eagle flow solver calculates the viscous terms explicitly and implements them after the inviscid terms have been calculated in an implicit upwind method. The inviscid portion of the algorithm optionally uses either flux-vector split or flux-difference split finite volume formulations. By computing the viscous terms explicitly, the cost of the thin-layer algorithm is only about 15% greater than the Euler algorithm on an identical grid. This is due to the separate calculation of the inviscid terms for which upwind differencing is most effective. Whitfield[5] developed the baseline algorithm with flux-vector splitting, and Gatlin and Whitfield[6] added the thin-layer approximation. The version of the Program Eagle flow solver used in this study was further modified by Simpson and Whitfield[7] to include a flux-difference splitting scheme due to Roe. The code includes the SuperBee, Minmod, and Van Leer limiters that act to suppress nonphysical oscillations near discontinuities.

Whitfield's two-pass factorization as used in the baseline algorithm is

$$(I + \Delta\tau\delta_\xi A^+ \cdot + \Delta\tau\delta_\eta B^+ \cdot + \Delta\tau\delta_\zeta C^+ \cdot)$$
$$\times (I + \Delta\tau\delta_\xi A^- \cdot + \Delta\tau\delta_\eta B^- \cdot + \Delta\tau\delta_\zeta C^- \cdot)\Delta Q^n$$
$$= -\Delta\tau(\delta_\xi F^n + \delta_\eta G^n + \delta_\zeta H^n) \quad (1)$$

Here A^+, B^+, etc., are the Jacobians of the split flux vectors; ΔQ is the vector of changes in the conserved variables; and $\Delta\tau$ is the computational time step; and F, G, and H include inviscid and viscous terms. This method has good stability properties as shown by Anderson[8] and is solved by forward substitution in the first pass and backward substitution in the second pass. The implicit solution can be vectorized on diagonal planes in computational space. The first pass can be thought of as beginning at one corner of the three-dimensional grid and sweeping through diagonal planes until the opposite corner is reached. The second pass begins at this corner and sweeps back to the first. It is simple to show that the factorization error from this method will not be symmetric for an initially symmetric flow unless $\Delta Q = 0$.

For this study a different approximate factorization (investigated by Anderson[8]) was used to ensure numerical symmetry in the crossflow plane. This was referred to as the combination factorization by Anderson and is given by

$$(I + \Delta\tau\delta_\xi A^+ \cdot + \Delta\tau\delta_\eta B^+ \cdot + \Delta\tau\delta_\eta B^- \cdot)$$
$$\times (I + \Delta\tau\delta_\xi A^- \cdot + \Delta\tau\delta_\zeta C^+ \cdot + \Delta\tau\delta_\zeta C^- \cdot)\Delta Q^n$$
$$= -\Delta\tau(\delta_\xi F^n + \delta_\eta G^n + \delta_\zeta H^n) \tag{2}$$

This results in two block-tridiagonal systems to be solved for the dependent variables:

$$(I + \Delta\tau\delta_\xi A^+ \cdot + \Delta\tau\delta_\eta B^+ \cdot + \Delta\tau\delta_\eta B^- \cdot)\Delta Q^*$$
$$= -\Delta\tau(\delta_\xi F^n + \delta_\eta G^n + \delta_\zeta H^n) \tag{3}$$

$$(I + \Delta\tau\delta_\xi A^- \cdot + \Delta\tau\delta_\zeta C^+ \cdot + \Delta\tau\delta_\zeta C^- \cdot)\Delta Q^n = \Delta Q^* \tag{4}$$

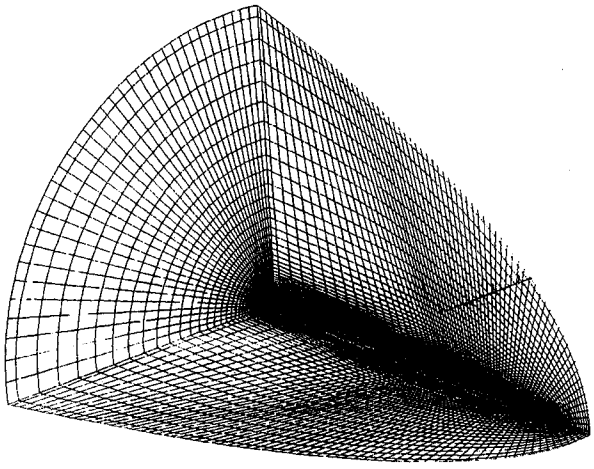

Fig. 1 Supersonic grid.

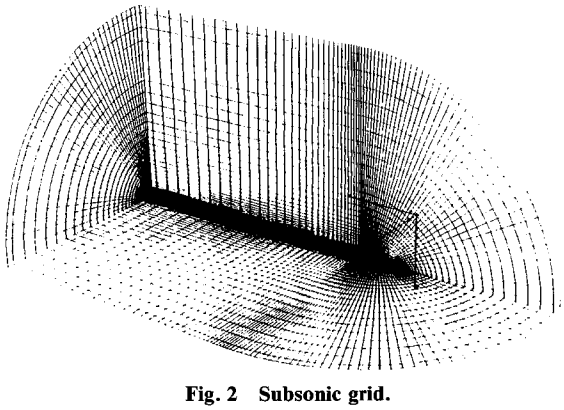

Fig. 2 Subsonic grid.

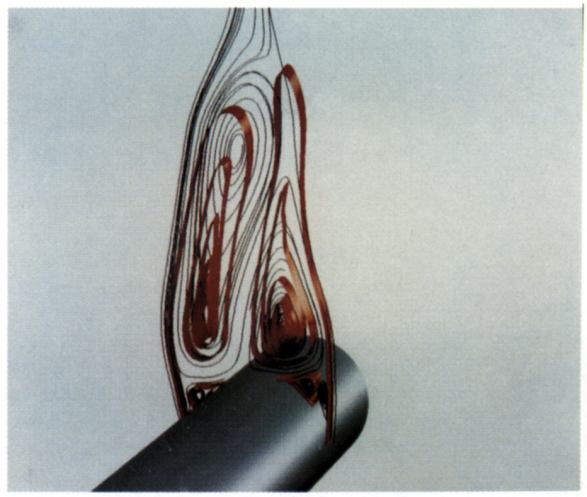

Fig. 3 $M = 1.4$ unsymmetric factorization, minmod without bump.

The first system was solved for each constant *ik* line in a crossflow plane while sweeping through the crossflow planes from upstream to downstream. The second system was solved for each constant *ij* ring in a crossflow plane while sweeping the crossflow planes from downstream to upstream. This approximate factorization and solution procedure yielded various ΔQ that were symmetric in the crossflow plane to 12 orders of magnitude given a perfectly symmetric grid and freestream initial conditions. None of the unlimited solutions with this approximate factorization ever developed asymmetry as opposed to the Whitfield or unsymmetric factorization of Refs. 4 and 7. Even with the symmetric factorization, however, the use of flux limiters resulted in magnification of asymmetries from the 10^{-12} initial level to 10^{-5} in one time step.

Body Configuration and Computational Grids

The configuration used for this paper is a 5.0 l/d tangent-ogive nose with a nose half-angle of 11.42 deg, which is connected to a circular afterbody 8 diameters long. The grids were generated using Program Eagle–Numerical Grid Generation System. The single block supersonic and subsonic grids each consist of 70 axial, 60 normal, and 101 circumferential points. The re-entrant boundary was located on the windward side of the body. The thin-layer Navier-Stokes solution on this grid took 55 million words of in-core memory on the Eglin Air Force Base Cray Y-MP supercomputer. The grid used was exactly symmetric between left and right sides except for the cases where a bump was deliberately introduced. Figure 1 shows the supersonic grid and Fig. 2 the subsonic grid.

Boundary Conditions

If the governing equations are cast in characteristic variable form, there will be an eigenvalue associated with each characteristic variable indicating the direction in which information is propagated across each constant computational surface. This is the basis for determining boundary conditions known as characteristic variable boundary conditions. This technique is implemented by a layer of phantom points surrounding the block boundaries at which the change in dependent variables is taken to be zero. Since these boundary conditions are treated explicitly, they are first-order accurate. Characteristic variable boundary conditions are employed at all far-field boundaries except downstream, where extrapolation is used. No-slip conditions are applied to the momentum terms at impermeable surfaces. The momentum values at the body surface are mirrored with negative values at the image point. This gives a zero momentum flux at solid wall boundaries. The normal temperature derivative is set to zero at the shearing surface for adiabatic wall conditions. The normal pressure gradient is

Fig. 4 $M = 1.4$ symmetric factorization, no limiter with bump.

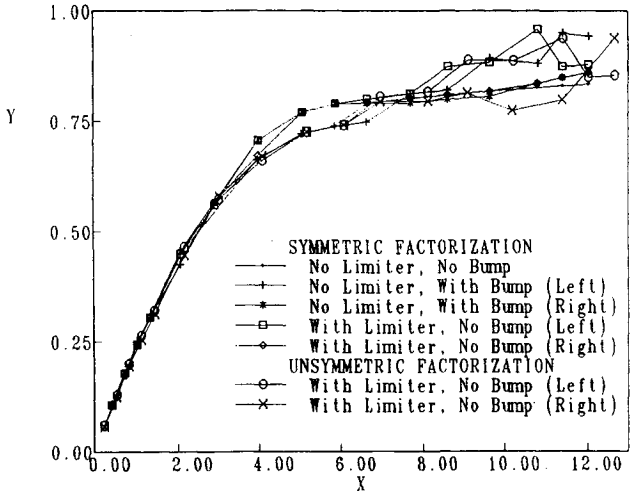

Fig. 5 $M = 1.4$ vortex core location.

assumed to be negligible at the wall to obtain values for energy and density.

Results

All of the results presented in this paper were computed with the second-order Roe flux-difference split option of the Eagle code. Various limiter options as well as the two factorizations presented earlier were used to compute flow solutions at 38.5 deg angle of attack, a Reynolds number of 2×10^5 based on maximum body diameter, and Mach numbers 1.4 and 0.60. Solutions were compared to evaluate the sensitivity of the flow structure to the numerical algorithm. For the solutions that remained symmetric, a perturbation was introduced and then removed to determine whether the development of asymmetry in supersonic flows is due to a convective-type instability as has already been observed in subsonic cases.

An important point to note is the sometimes large disparity between constrained two-dimensional particle traces and the clipped views of true three-dimensional separation sheets. The two-dimensional traces were often misleading. A prime example is shown in Fig. 3 for unsymmetric factorization with minmod limiter. The two-dimensional particle traces show the left vortex position to be much farther away from the body than it actually is. The correct vortex position is indicated by the clipped three-dimensional separation sheet colored red. It is interesting to note that the two-dimensional particle traces do agree with the three-dimensional separation sheet for the right vortex. Caution must be used when using constrained particle traces. Conditions required for a good match are that the vortex core be straight and perpendicular to the cross section in which the two-dimensional traces are plotted.

Supersonic

It was found that both factorizations, when using limiters, always converged toward an asymmetric solution on a symmetric grid at 38.5 deg. However, the symmetric factorization without a limiter converged to a solution that was symmetric to 12 orders of magnitude. This solution was converged to machine zero and then run for an additional 15,000 iterations. All other supersonic results in this study were converged to 6 orders of magnitude. This solution was then restarted on a grid with a bump to determine if the flow would be perturbed into an asymmetric state. This bump was located at a circumferential angle of 90 deg and 0.01 maximum body diameter back from the nose and had a height of 0.01 maximum body diameter. The extremely small relative size of the bump is apparent from the enlargement of the nose region in Fig. 4. After the introduction of the bump, the solution reconverged to an asymmetric flow. This was then repeated with the bump being placed at a circumferential angle of 270 deg with the resulting flow solution being a mirror image of that obtained with the bump at 90 deg. The bump was then removed from the grid, and the solution reconverged back to the original symmetric flow. Figures 5 and 6 are plots of vortex core location as determined by finding the minimum in total pressure for some of the cases discussed earlier. The ratio of the total pressure to freestream pressure in the core is shown in Fig. 7.

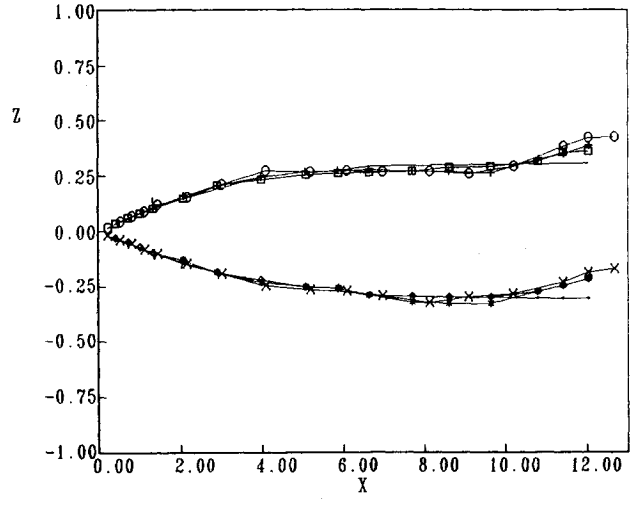

Fig. 6 $M = 1.4$ vortex core location.

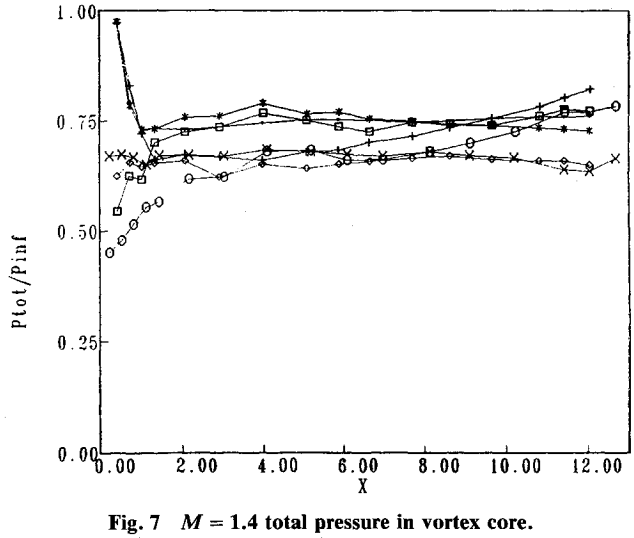

Fig. 7 $M = 1.4$ total pressure in vortex core.

Figures 8 and 9 show the flow structure at 38.5 deg calculated using unsymmetric factorization. Two-dimensional particle traces (white) are shown at the rear of the tangent-ogive nose (x/d 5), and the limiting streamlines are shown on the body nose (red). The density contours are also shown at the rear of the nose. The three-dimensional primary, secondary, and tertiary vortices are shown in green, cyan, and yellow, respectively. The two-dimensional crossflow particle traces were computed by setting the u momentum equal to zero, and the limiting streamlines were obtained by converting the velocity vectors to tangential components in a two-dimensional parametric coordinate system. The scale used for all nondimensionalized density contours, unless otherwise noted, is 0.2 at black and 1.5 at white with equal bands from blue to cyan to green to yellow to red to magenta to white. Cross sections of the three-dimensional separation surfaces were obtained by injecting particles along the separation lines as indicated by the limiting streamlines. Surfaces were then constructed by integrating particle paths. Examples of the three-dimensional particle traces that make up the three-dimensional separation surfaces are shown in Figs. 8 and 9 in the same color as their corresponding surface. Cross sections were obtained by clipping the surface formed in this manner between two constant axial coordinate planes. Another vortex was observed very close to the body surface and is illustrated by yellow three-dimensional particle traces. Near the rear of the body the flow develops substantial asymmetry. This asymmetry is present over the length of the body as illustrated by the green separation surface on the right side of the nose in Figs. 8 and 9

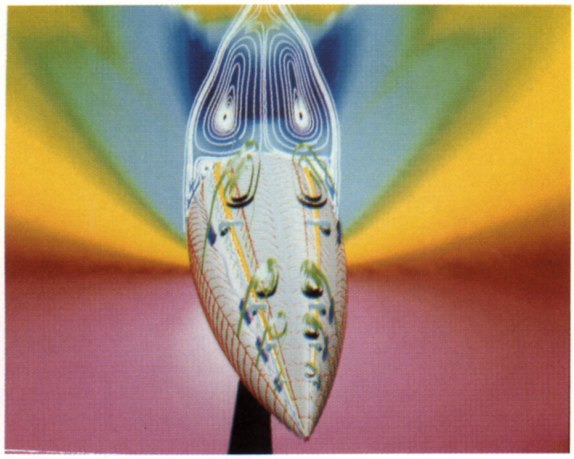

Fig. 8 $M = 1.4$ unsymmetric factorization, minmod without bump.

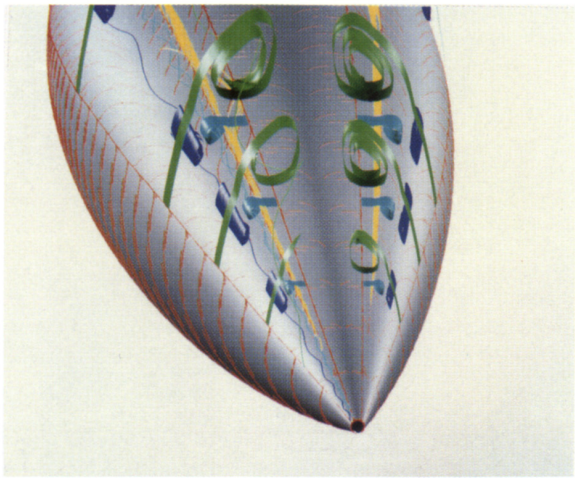

Fig. 9 $M = 1.4$ unsymmetric factorization, minmod without bump.

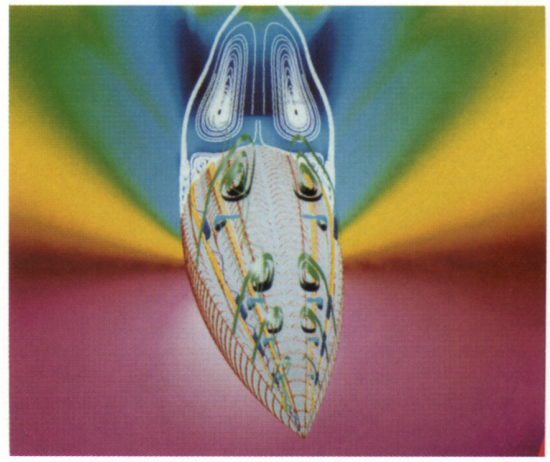

Fig. 10 $M = 1.4$ symmetric factorization, no limiter without bump.

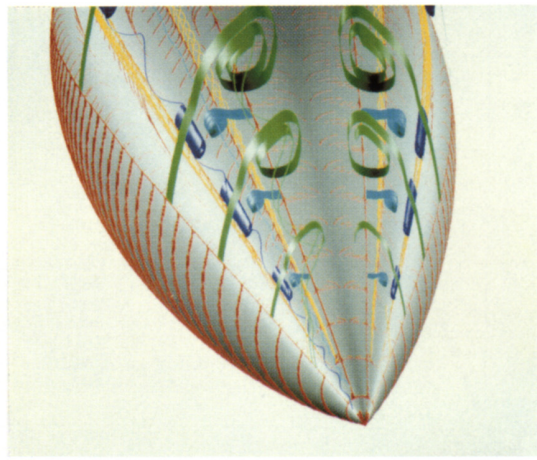

Fig. 11 $M = 1.4$ symmetric factorization, no limiter without bump.

already showing a noticeably tighter roll-up. The vortex shown by the dark blue is fed from particles injected over a very small region of the primary separation line near the tip. The asymmetry in the size of this region is the cause of the initial asymmetry in the primary vortex roll-up.

Figures 10 and 11 show the same view for the symmetric factorization before the introduction of the bump. Figures 4 and 12 show the flow after the introduction of the bump. The flow on the side of the bump is less defined. The three-dimensional particle traces can be seen to be more erratic than in the two previous cases. There was a great deal of mixing between the different vortices on the bump side compared with the other side. Note the most leeward yellow particle traces on the bump side. They are initially tightly coiled, then rapidly spread apart due to the bump's perturbation of the flow. Downstream of the region the vortex becomes tightly coiled once again. Note that there are blue regions in the primary vortex separation sheet cross sections (green). This is because, unlike the other cases and the right-hand side of this case, the blue vortex is not isolated from the rest of the flow. Whereas before particle traces entered and stayed in the dark blue vortex, they now leave and enter other vortices.

Figure 13 shows a series of cross-sectional density contours near the tip of the tangent-ogive nose. The scale is from 0.1 to 1.5. The bump is clearly shown by the middle contour ring. The height of this bump, as mentioned before, is only 1% of the maximum body diameter. The smallest density contour ring, being in front of the bump, shows that the flow was initially very symmetric. The third density contour cross section, although very close to the region of the nose containing

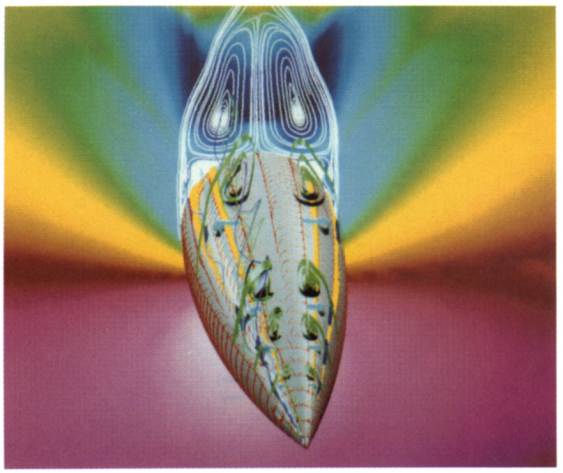

Fig. 12 $M = 1.4$ symmetric factorization, no limiter with bump.

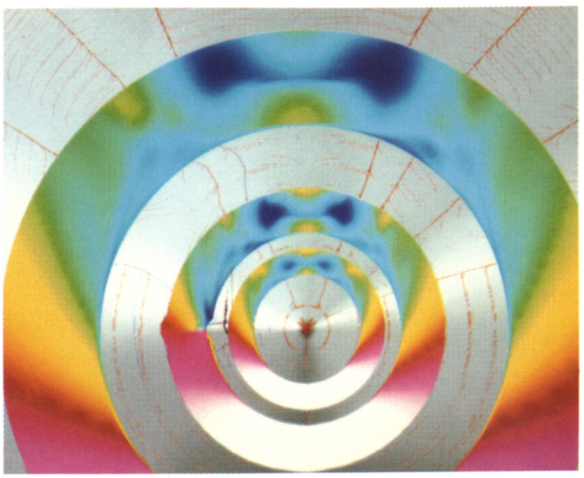

Fig. 13 $M = 1.4$ symmetric factorization, no limiter nose region with bump.

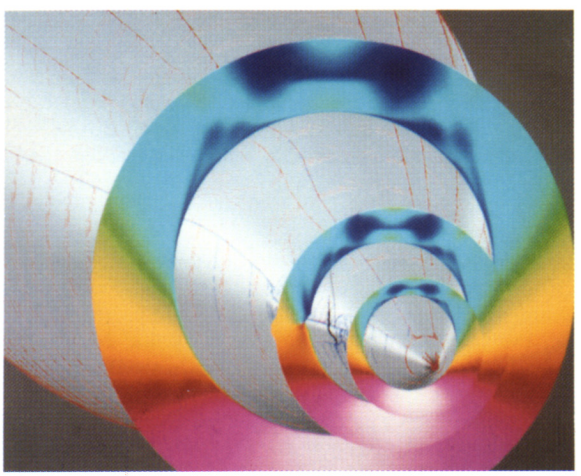

Fig. 14 $M = 1.4$ symmetric factorization, no limiter nose region with bump.

the bump, already shows the leftmost primary vortex having moved farther away from the body than the right one. Figure 14 shows another view of the density contours near the bump but with more detail of the limiting streamlines near the bump. It was observed that one of the limiting streamline convergence lines went from the nose tip down along the surface of the body until it came to the bump, at which point it bent toward the bump. It ran along the opposite side of the bump until clear and then resumed its original position along the distance of the body. Figures 15 and 16 show the vortex cores over the full length of the body from the top and side, respectively. The vortex core can be seen to waver near the bump and begin to bend near the rear of the body.

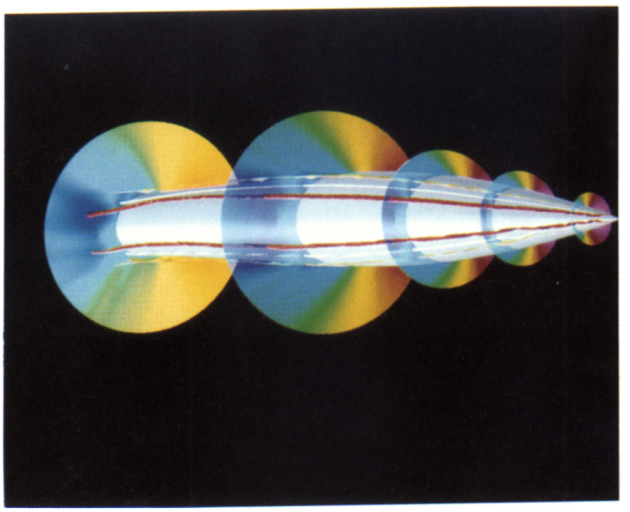

Fig. 15 $M = 1.4$ symmetric factorization, no limiter with bump.

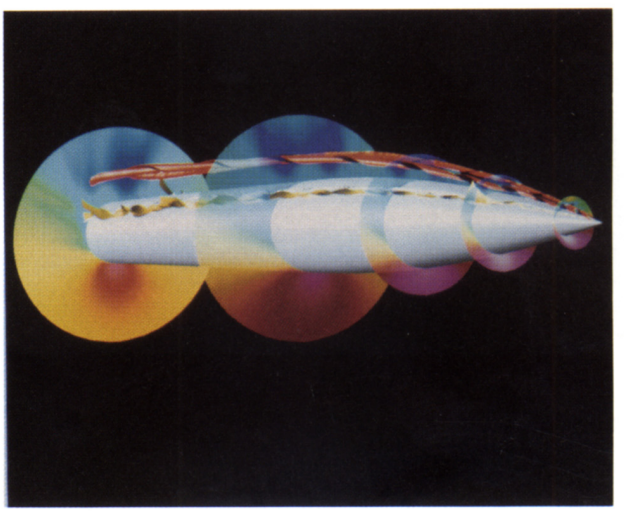

Fig. 16 $M = 1.4$ symmetric factorization, no limiter with bump.

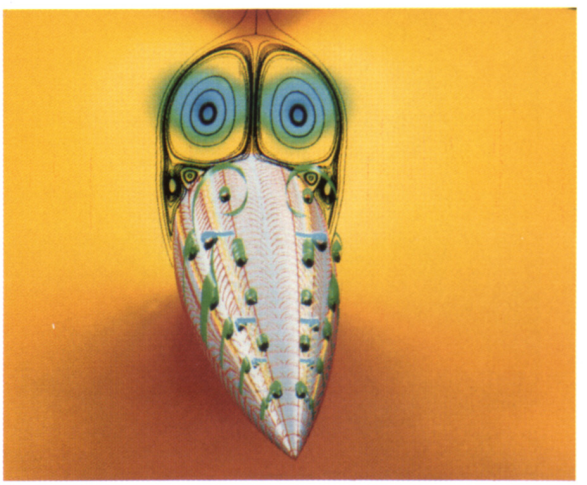

Fig. 17 $M = 0.6$ symmetric factorization, no limiter without bump.

Subsonic

A Mach = 0.6, 38.5-deg case was computed with the symmetric factorization. Figure 17 shows the nose region. This case maintained symmetry to 12 orders of magnitude, while the residual dropped 3 orders of magnitude. The density contour scale here is from 0.5 to 1.25. A major difference between this case and the supersonic case discussed earlier concerns the outer most secondary vortex. It was mentioned before that for the supersonic case particle traces could only be found entering this vortex at the tip of the nose for a short distance. Instead, for the subsonic case, three-dimensional particle traces feed the primary core for a while until the separation surface kinks and rolls up in the smaller vortex for a while. Here the primary vortices and the secondary vortices that they feed are colored green. Figure 18 shows a close-up view of the nose region in which two smaller vortices (yellow) can be seen on each side. The flow structure remains basically the same over the remaining length of the body as shown in Figs. 19 and 20. The primary vortices do not move away from the body significantly.

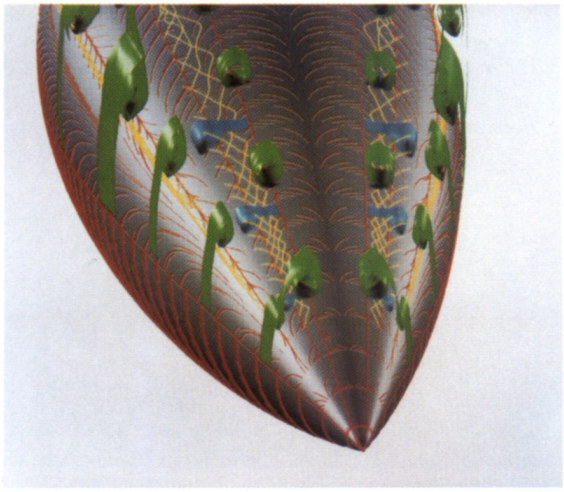

Fig. 18 $M = 0.6$ symmetric factorization, no limiter without bump.

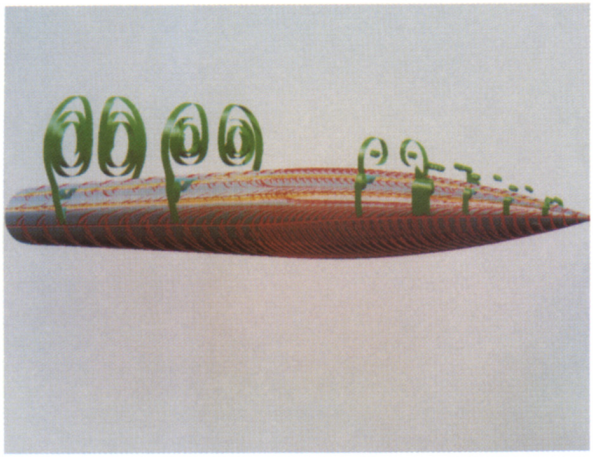

Fig. 19 $M = 0.6$ symmetric factorization, no limiter without bump.

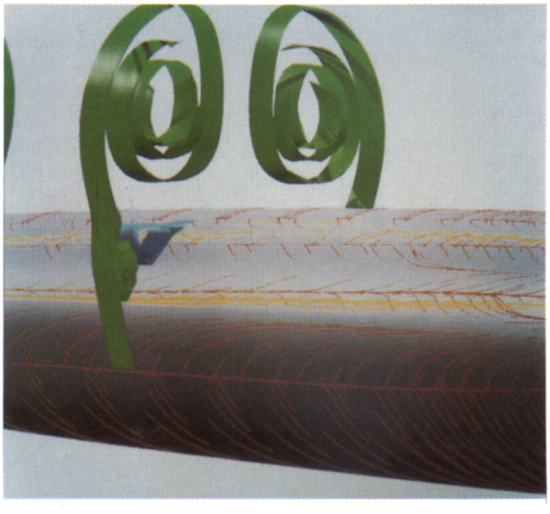

Fig. 20 $M = 0.6$ symmetric factorization, no limiter without bump.

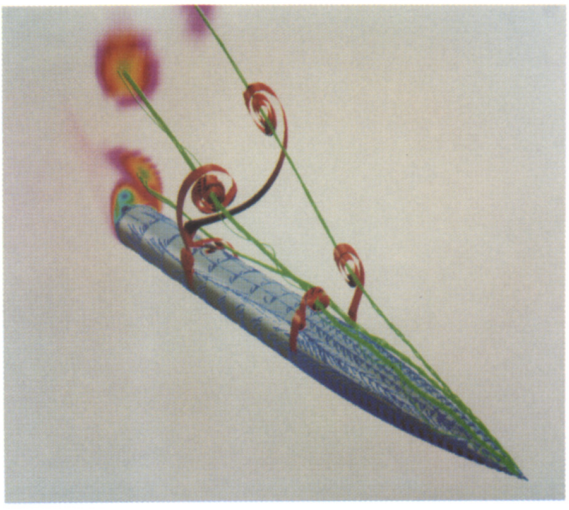

Fig. 21 $M = 0.6$ symmetric factorization, no limiter with bump.

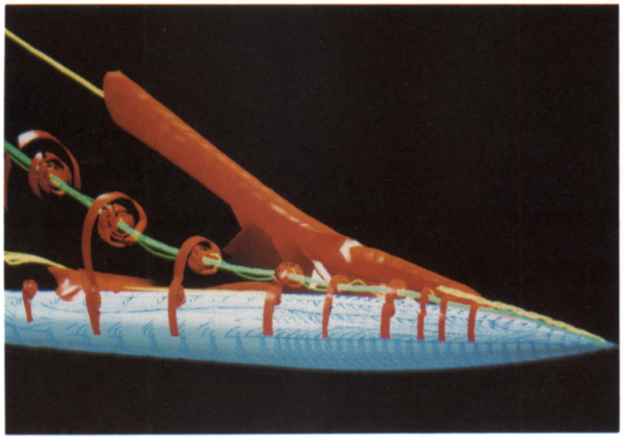

Fig. 22 $M = 0.6$ symmetric factorization, no limiter with bump.

A bump was introduced for the subsonic case, and the flow was observed to go asymmetric. Figure 21 shows the massive asymmetry that occurs for this case. Unlike the supersonic case, the vortices depart from the body and begin to alternately shed from the left and right sides of the body. Figure 21 gives the three-dimensional surface cross sections showing the first such pair. Total pressure is plotted near the back plane of the 13 caliber body showing the second set of vortices forming. Figure 22 shows the same flow with one primary separation sheet instead of clipped cross sections. When the bump is removed from this subsonic case, the flow begins to regain symmetry. By the time the original convergence level is regained, the flow is symmetric to three orders of magnitude.

Conclusions

The supersonic and subsonic asymmetric vortical flow on a tangent-ogive body has been computed using both unsymmetric and symmetric factorizations. It was found that the unsymmetric factorization with limiters contained enough numerical error to induce asymmetry in the vortical flow without any

special perturbation. The symmetric factorization without limiter needed the introduction of a geometric imperfection (bump) on the nose before the solution would become asymmetric for either subsonic or supersonic flow. The flow reconverged to a symmetric state when the bump was removed. The unsymmetric factorization with minmod and the symmetric factorization with Van Leer yielded the same topology but differed in vortex core location and total pressure in the core. Both limiter runs differed with the unlimited symmetric factorization with bump in both topology and vortex core location and the associated total pressure. The flow topology differed between the supersonic and subsonic cases studied. The primary separation sheet interacts much more strongly with the smaller vortex core near the surface in the subsonic case.

Acknowledgments

The authors would like to thank Ray Maple and Tim Stong for their help with the graphics software and figure preparation, respectively.

References

[1]Degani, D., "Numerical Investigation of the Origin of Vortex Asymmetry," AIAA Paper 90-0593, Jan. 1990.

[2]Chapman, G. T., and Tobak, M., "Nonlinear Problems in Flight Dynamics," NASA-TM-85940, May 1984.

[3]Siclari, M. J., "Asymmetric Separated Flows at Supersonic Speeds," AIAA Paper 90-0595, Jan. 1990.

[4]Vanden, K. J., "Thin-Layer Navier-Stokes Solutions of the Asymmetric Vortical Flow on a Tangent Ogive Body," M.S. Thesis, Univ. of Florida, Gainsville, FL, 1989.

[5]Whitfield, D. L., "Implicit Upwind Finite Volume Scheme for the Three-Dimensional Euler Equations," Mississippi State Univ., Rept. MSSU-EIRS-ASE-85-1, Mississippi State, MS, Sept. 1985.

[6]Gatlin, B., and Whitfield, D. L., "An Implicit, Upwind, Finite-Volume Method for Solving the Three-Dimensional Thin-Layer Navier-Stokes Equations," AIAA Paper 87-1149, June 1987.

[7]Simpson, L. B., and Whitfield, D. L., "A Flux Difference Split Algorithm for Unsteady Thin-Layer Navier-Stokes Solutions," AIAA Paper 89-1995, June 1989.

[8]Anderson, W. K., "Implicit Multigrid Algorithms for the Three-Dimensional Flux Split Euler Equations," NASA-CR-179742, Aug. 1986.